

# Characterization of radiative heat transfer in a spark-ignition engine through high-speed experiments and simulations

Lucca Henrion<sup>1,\*</sup>, Michael C. Gross<sup>2</sup>, Sebastian Ferrery Fernandez<sup>3</sup>, Chandan Paul<sup>3</sup>, Samuel Kazmouz<sup>3</sup>, Volker Sick<sup>1</sup>, and Daniel C. Haworth<sup>3</sup>

<sup>1</sup>Department of Mechanical Engineering, University of Michigan, 1231 Beal Ave, Ann Arbor, MI 48109, USA

<sup>2</sup>Southwest Research Institute, 4622 Runway Blvd, Ann Arbor, MI 48108, USA

<sup>3</sup>Department of Mechanical Engineering, Pennsylvania State University, 140 Research Building East, University Park, PA 16802, USA

Received: 14 January 2019 / Accepted: 2 May 2019

**Abstract.** A combined experimental and Large-Eddy Simulation (LES) study of molecular radiation is presented for combustion in a homogeneous pre-mixed spark-ignition engine. Molecular radiation can account for ~10% of the engine heat loss and could have a noticeable impact on the local conditions within the combustion chamber. The Transparent Combustion Chamber (TCC) engine, a single-cylinder two-valve research engine with a transparent liner and piston for optical access, was used for this study. High-speed infrared emission spectroscopy and radiative post-processing of LES calculations have been performed to gain insight into the timescales and magnitude of radiative emissions of molecular gases during the combustion process. Both the measurements and simulations show significant Cycle-to-Cycle Variations (CCV) of radiative emission. There is agreement in the instantaneous radiative spectrum of experiment and simulation, but the crank-angle development of the radiative spectrum shows disagreement. The strengths and limitations of the optical experiments and radiative simulations are seen in the results and suggest pathways for future efforts in characterizing the influence of molecular radiation. In particular, focusing on the relative changes of the spectral features will be important as they contain information about the thermochemical properties of the gas mixture.

## 1 Introduction

Seventy percent of the crude oil used worldwide is consumed by Internal-Combustion (IC) engines [1]. Regulations demand increased efficiency and reduced pollutant emissions in the next generation of spark-ignition engines. One pathway to improving efficiency is operating at higher pressures, but increasing pressure raises heat loss due to higher gas temperatures. Additionally, higher operating temperatures yield increased NO<sub>x</sub> formation. Exhaust-Gas Recirculation (EGR) is used to mitigate NO<sub>x</sub> production and reduce the peak in-cylinder temperatures [2]. Predictive Computational Fluid Dynamics (CFD) simulations can be used to rapidly optimize these types of efficiency trade-offs; however, the development of accurate simulations must be closely followed with validation through collaborative and comprehensive experiments. CFD modeling can be used to evaluate the impact of changing operating schemes and, most relevant to this work, track the flux of energy throughout the chamber and out of the boundaries.

The different modes of heat transfer must be considered when modeling engine heat loss. Previous research has shown that radiation is a significant contributor to engine heat loss in heavy-duty diesel engines, where it was suggested that soot radiation could increase wall heat-flux by 40% and reduce NO<sub>x</sub> emission by 46% [3, 4]. The molecular radiation of H<sub>2</sub>O and CO<sub>2</sub>, which occurs primarily in the Infrared (IR) band, has been considered unimportant to engine heat transfer [5]; soot was considered the dominant source of radiative heat transfer in Compression Ignition (CI) engines [6]. The impact of radiation on vehicle-scale engines, especially in Spark-Ignition (SI) engines, has not been studied with CFD modeling.

Recently, the use of advanced modeling techniques such as the Photon Monte Carlo method/Line-by-Line (PMC/LBL) and full-spectrum *k*-distribution have shed light on the impact of radiation and the importance of molecular radiation in particular [7–10]. Indeed, simulations of a CI engine have demonstrated that more molecular emission than soot emission reaches the wall [10], and the relative contribution of molecular radiation will be much higher in SI engines, where substantially less soot is produced.

\* Corresponding author: [lhenrion@umich.edu](mailto:lhenrion@umich.edu)

The emission spectra of soot incandescence and molecular radiation are qualitatively different. Soot radiates as a near-ideal blackbody, emitting over a broad wavelength range determined entirely by its temperature, while molecular radiation emits and absorbs over narrow wavelength bands. Reabsorption of emitted energy also differs between molecular and soot emission. For example, CO<sub>2</sub> emission is the dominant component of the total radiative emission, but most of this emission is reabsorbed before reaching the engine wall, leading to energy redistribution [7]. Simulations of high-pressure turbulent flames have shown that >80% of emitted radiation can be reabsorbed before reaching the flame boundary [7]. Therefore, these molecular emissions may have a significant impact on wall heat loss and a noticeable influence on energy redistribution within the combustion chamber.

This energy redistribution would be more pronounced with the addition of EGR. EGR consists principally of inert gases (H<sub>2</sub>O and CO<sub>2</sub>) that are strong emitters and absorbers in the Infrared (IR) band. The resulting energy redistribution can lead to changes in local temperatures of tens of K [10]. Meanwhile, increasing engine efficiency requires operating closer to the limits of stable combustion, where slight changes in local conditions are important. Simulations that capture Cycle-to-Cycle Variation (CCV) must be utilized to examine small changes in local conditions between cycles, and to determine the impact of radiation over multiple cycles.

Experiments studying IR features in combustion systems are numerous, and significant research has been invested to develop measurement methods that can accurately determine flame temperature and molecular concentrations [11]. However, many of these experiments measure the emission or absorption across a narrow wavelength range. Simulations demonstrate that >90% of CO<sub>2</sub> and H<sub>2</sub>O emission occurs from 1 to 6 μm, but few experiments have measured the in-engine emission and absorption of combustion products across micron wavelength ranges. Experiments performed by Rein *et al.* demonstrated a methodology to measure IR emission and absorption across a large wavelength range using Fourier Transform Infrared (FTIR) spectroscopy [12–14]. However, these measurements have not yielded time-resolved results to compare with Large-Eddy Simulations (LES), where CCV is captured. To overcome these limitations, we developed an experimental technique that captured spectral radiation at crank-angle temporal resolutions across a large wavelength range [15]. The radiative variation is of particular importance, as the upper limit of radiation may cause local temperature changes that impact engine operation. Therefore, this work presents the first coupling of experiments and simulations of engine radiative emissions, demonstrates validation of the simulations, and evaluates the importance of molecular emission in spark-ignition engines.

The next generation of engine simulations must incorporate quantitative models of molecular radiation and reabsorption. PMC/LBL is the current benchmark for accurate radiation modeling; it has been used to check the accuracy of less computationally expensive models [9]. However, PMC/LBL has not been validated with measurements

from in-engine experiments. Spectral interdependence, Turbulence-Radiation Interactions (TRI), and radiative trapping influence experimental measurements of spectral emissions. The widespread implementation of these radiative models must be prefaced with experimental validation. We present the development and results of a collaborative experimental/simulation study of the spectral emissions of combustion products within an optically accessible SI engine. This combination provides detailed information about intra- and trans-cylinder radiative heat transfer.

## 2 Experimental method

### 2.1 Optically accessible engine

The engine used for both experiments and simulations was the third-generation Transparent Combustion Chamber (TCC-III) engine [16]. The engine is a two-valve, four-stroke, pancake-style chamber with a bore × stroke of 92 mm × 86 mm, and a 10:1 geometric compression ratio. A central spark plug ignited a homogeneous and stoichiometric mixture of propane/air heated to 95 °C at the intake. The engine ran at 1300 rev/min. The ignition timing was −18° after top dead center compression (°aTDC); in other words, 18° before top dead center. An in-cylinder piezo-electric pressure transducer (Kistler 7001) was sampled every 0.5 Crank-Angle Degrees (CAD) to measure the intra-cycle pressure dynamics. Additional piezo-resistive pressure transducers (Kistler) were located in the intake and exhaust systems to set the desired boundary conditions of an intake pressure of 40 kPa and an exhaust pressure of 98 kPa. The air and fuel flow were metered using critical-flow nozzles. Data describing the geometry of the TCC-III engine and the GT-Power model are available for download at <https://deepblue.lib.umich.edu/handle/2027.42/108382>.

The variability in the different test runs is important, because the differences in peak pressure and Indicated Mean Effective Pressure (IMEP) lead to differences in the spectral signal. The average peak pressure for all the recorded runs is 1835.3 kPa with a maximum relative deviation between runs of 1.8%. Similarly, the relative variation of IMEP between separate recorded runs was up to 2.4%. These discrepancies are small compared to the differences seen between the measured and simulated pressure dynamics.

Optical access was provided through a fused-silica cylinder. The transmission of this material varies according to the manufacturing process, so the transmission of this fused silica cylinder was measured. The cylinder offers excellent transmission in the visible through near-infrared bands, but its transmission is poor at ~2.8 μm and beyond ~3.7 μm, as seen in Figure 1. This transmission curve was used to correct for the non-uniform transmission at different wavelengths, and it was used to determine the wavelength region measured during the presented study. Given the poor and non-uniform transmission in wavelengths greater than 2.8 μm, all measurements presented within this document were recorded in the 1.4–2.81 μm region.

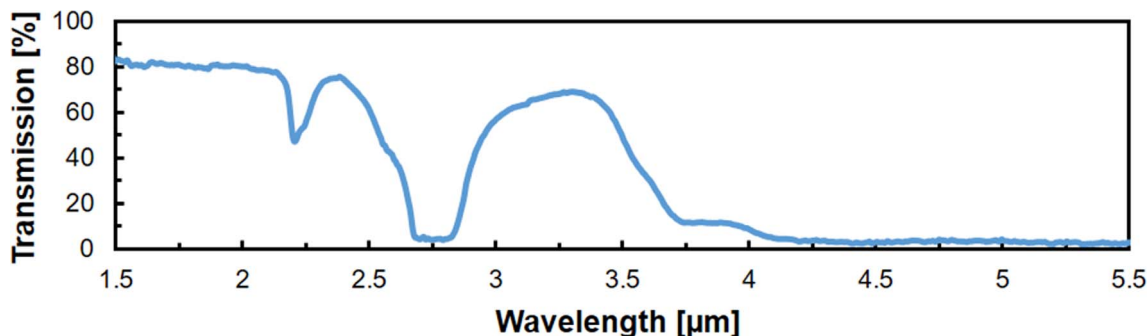


Fig. 1. The transmission spectrum of the fused-silica cylinder

## 2.2 Crank-angle-resolved infrared spectroscopy

A grating spectrometer (McPherson Model 2035) with two turret-mounted infrared gratings was used to disperse the IR radiation from the engine, as diagrammed in Figure 2. The experimental data shown in the results section was captured using a grating that was blazed at 2.1  $\mu\text{m}$  with a density of 30 grooves/mm. An output mirror with a 400-mm focal length was used to place the output image on the image sensor of the camera. All internal mirrors were coated in gold to provide uniform reflection across the wavelengths investigated.

Focusing optics (two  $\text{CaF}_2$  plano-convex lenses with focal lengths,  $f$ , of 250 mm and diameters of 50 mm) focused the radiation emitted from the combustion within the optical engine onto the entrance slit of the spectrometer. The focusing optics were located such that the focal point was placed at the center of the cylinder and 10 mm below the cylinder head. This technique is a passive one – there is no illumination – therefore, all of the radiation within the volume accessible from the focusing optics was recorded in the spectra.

A broadband high-speed infrared camera (*Xenics Onca MWIR InSb 320*) sensitive from 1.0 to 5.5  $\mu\text{m}$  was coupled to the IR spectrometer to measure the spectrum. The Onca camera has an indium antimonide (InSb) image sensor with  $256 \times 320$  pixels and 14 bits of dynamic range. The sensor is cryogenically cooled with a Stirling cooler so that radiation from this wavelength range can be measured. The camera can record at 460 Hz full frame; however, for spectroscopic measurements, only horizontal information was needed to resolve wavelengths. Therefore, these measurements were made with the camera operating with only  $8 \times 320$  active pixels, allowing frame rates up to 4.0 kHz. However, a cold shield aperture protecting the image sensor obstructs the signal of 132 columns of pixels. Signal from those columns was discarded, leaving 188 pixels in the center of the image sensor to measure the spectrum. The camera was operated with 72- $\mu\text{s}$  integration times to allow fast repetition rates and best usage of the full dynamic range of the camera. A two-brightness nonuniformity correction was performed using an integrating sphere (*Electro Optical Industries ISV-400S*) and the Xenics Xeneth software.

A pixel-to-wavelength mapping was performed using the emission spectrum of a xenon-gas spectral-calibration

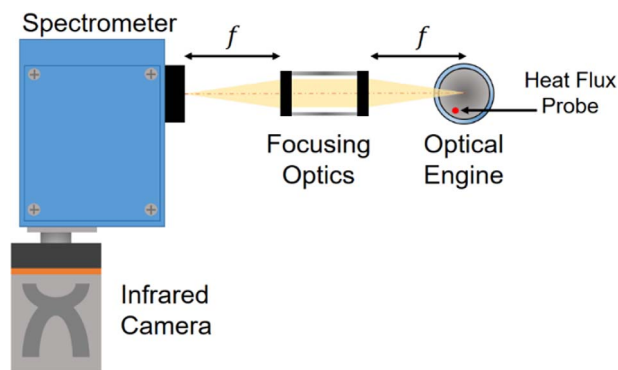


Fig. 2. Schematic of experimental apparatus for spectral measurements in TCC-III engine.

lamp (Newport 6033) [17]. Two emission lines separated by  $\sim 12$  nm were used to measure the single-shot span and the spectral resolution of the setup. With the grating described, the spectrometer produced spectra with  $\sim 4$ -nm spectral resolution (FWHM at 1959.94 nm) and a span up to 460-nm.

Heat flux measurements were made with a heat-flux probe (Medtherm TCS-233-JU(JU-.156)-72-11340). This probe was located 35.5 mm from the measurement axis, as seen in Figure 2. One thermocouple was set at the probe surface and another was set at 3.96 mm into the probe material. A complete description of the heat-flux probe and measurement protocol within the TCC-III engine was provided in [18]. The instantaneous heat flux was calculated from the surface temperature probe and the recessed temperature probe following a procedure described in [19]. The uncertainty of these measurements showed a standard error of around 5% [18].

## 2.3 Experimental post-processing

Background emission is present in all measurements due to the length of exposure. After recording, the raw data was corrected for the influence of background emission using spectra that were recorded from the motored engine without fueling. The background spectrum is the average spectrum of the motored measurements from  $-150$  to  $-130$   $^\circ\text{aTDC}$  for the first measured cycle where only

background signal is present. The resulting background spectrum,  $B_\lambda$ , was subtracted from the raw measured spectrum,  $I_{CA,\lambda}^{\text{raw}}$ . Previous experiments have shown that compression of the fuel and residual  $\text{H}_2\text{O}$  and  $\text{CO}_2$  produces appreciable emission; this emission was not removed from the measured spectra.

The spectral influence of the experimental apparatus on measurements was corrected using a spectral-response curve measured with a blackbody source (*Electro Optical Industries* LES800-04). A broadband spectrum (from 1 to 5.5  $\mu\text{m}$ ) of the blackbody source was measured with the source at 20 °C (room temperature) and at 800 °C. The 20 °C spectrum was treated as the background emission and subtracted from the 800 °C spectrum to create a measured blackbody curve. Planck's law of blackbody radiation was used to calculate a theoretical blackbody spectrum at 800 °C, and the non-blackbody emission of the blackbody source was corrected through an emissivity spectrum provided by the source's manufacturer. The measured blackbody spectrum was then divided by the theoretical blackbody spectrum to create the spectral response curve,  $S_\lambda$ . An important component of the non-uniform spectral response curve is the strong atmospheric absorption by  $\text{H}_2\text{O}$  and  $\text{CO}_2$  in the relevant wavelengths. Atmospheric absorption depends on the path length between the combustion chamber and the image sensor, which was around 150 cm in the experimental setup. The impact of atmospheric absorption, grating efficiency, image-sensor efficiency, and the absorption of the optics in the experimental apparatus were corrected for with the resulting spectral-response curve.

Finally, the transmission of the fused-silica cylinder was measured using the blackbody source and a sample of the cylinder; the resulting curve,  $\tau_\lambda$ , allowed for correction of the transmission losses in the measured spectra. Figure 1 shows the transmission curve used to correct the data. The correction procedure is shown mathematically in the following equation, where  $I_{CA,\lambda}$  is the corrected spectral data. It is important to note that  $B_\lambda$ ,  $S_\lambda$ ,  $\tau_\lambda$  are all assumed constant in time, however, the spectral emission measurements vary in Crank Angle (CA).

$$I_{CA,\lambda} = \frac{I_{CA,\lambda}^{\text{raw}} - B_\lambda}{S_\lambda \times \tau_\lambda}$$

## 2.4 Measurement conditions

Given the measured transmission of fused-silica, all measurements were made from 1.4 to 2.81  $\mu\text{m}$ . However, even in this measurement region, the transmission correction sharply affects features as the low transmission amplifies the emission through the correction procedure. Since each measurement can only capture a 0.46- $\mu\text{m}$  range, three wavelengths regions were chosen. These wavelengths regions capture relevant  $\text{CO}_2$  and  $\text{H}_2\text{O}$  vibrations [20], as shown in Table 1. With the engine operated at 1300 rev/min, the high-speed spectral measurements yield spectra with a two-CAD resolution, and therefore measurements from  $-150$  to  $180$  °aTDC provided 166 spectra per cycle. Each wavelength range was measured for 100 continuous cycles.

## 3 Simulation setup

### 3.1 Large-Eddy Simulations

Large-Eddy Simulations (LES) have been performed using STAR-CD. Key features of the models are a Smagorinsky subfilter-scale turbulence model, a simple energy-deposition spark-ignition model, and a modified thickened flame model for turbulent flame propagation. Radiative heat transfer was not considered. Details can be found in [21]; the present LES model is referred to there as "Model 1." Sixty cycles (three blocks of 20 consecutive cycles each) were simulated using Model 1. LES Model 1 results were compared with those from a different LES model ("Model 2") and with experimental measurements to generate new physical insight into the early stages of combustion.

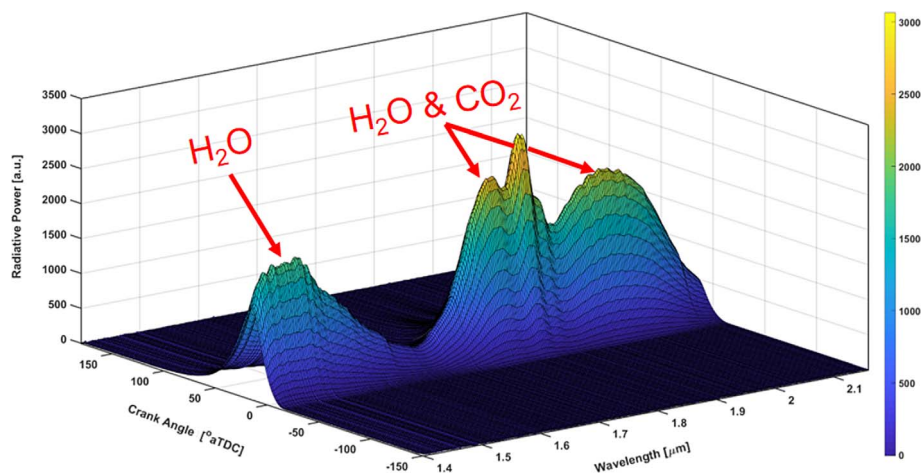
### 3.2 Radiative heat transfer post-processing

Here a subset of 19 consecutive Model 1 LES cycles from [21] is studied further to characterize in-cylinder radiative heat transfer, including quantitative comparisons between computed and measured spectral IR radiative intensities. The analysis is done in a post-processing mode, where instantaneous snapshots of computed three-dimensional fields of pressure, temperature, and radiatively participating species ( $\text{H}_2\text{O}$  and  $\text{CO}_2$ ) are used to compute the corresponding fields of radiative emission and reabsorption. The radiation post-processing tools are implemented in OpenFOAM [22]. The STAR-CD fields are interpolated to an OpenFOAM-compatible mesh, where the OpenFOAM mesh has an approximately uniform prescribed mesh spacing. Different combinations of spectral models and Radiative Transfer Equation (RTE) solvers are used to determine which aspects of the radiation modeling are most important in a spark-ignition engine. Results are compared at different instants in time, corresponding to different stages in the flame propagation process. Radiation fields corresponding to the ensemble-averaged mean fields of pressure, temperature, and radiatively participating species are compared with those corresponding to individual cycles to investigate cycle-to-cycle variations. And the OpenFOAM mesh resolution is varied to explore the influence of spatial scales on computed radiation fields.

In [23] a comprehensive modeling study of radiative heat transfer was reported for a heavy-duty diesel engine. There 10 different combinations of spectral models and RTE solvers were considered. Here three of the model combinations included in [23] are considered, plus a new simplified spectral model proposed recently in [9]. The four radiation models are: a stochastic Photon Monte Carlo method with Line-by-Line spectral resolution (PMC/LBL); a lowest-order spherical harmonics method (a P1 method) with a Full-Spectrum  $k$ -distribution spectral model (P1/FSK); a P1 method with a Gray (P1/Gray) radiation properties model; and the P1/Stepwise-Gray (P1/SWG) spectral model from [9]. In all cases, the latest available spectral database has been used for radiative properties [24], so that radiative emission is identical for all four models, by construction. The four models differ only in their calculation of radiative reabsorption.

**Table 1.** Spectroscopic locations measured and associated vibrations.

Experiment	Wavelength start ( $\mu\text{m}$ )	Wavelength end ( $\mu\text{m}$ )	H <sub>2</sub> O vibration	CO <sub>2</sub> vibration
EXP1	1.4	1.7	$\nu_1 + \nu_3, 2\nu_2 + \nu_3$	
EXP2	1.7	2.16	$\nu_2 + \nu_3$	$4\nu_2 + \nu_3, \nu_1 + 2\nu_3 + \nu_3$
EXP3	2.35	2.81	$\nu_3$	

**Fig. 3.** Phase-averaged emissions from EXP1 and EXP2. Vibrational bands are labeled with their constituent molecules.

PMC/LBL provides a benchmark against which the performance of simpler spectral models and/or RTE solvers can be compared. It is also the only model from which detailed quantitative radiative spectra can be extracted for comparison with the experimentally measured spectra. A comparison of results from PMC/LBL with those from P1/FSK reveals the extent to which the P1 RTE solver is sufficient for computing reabsorption, since the FSK spectral model gives results that are within approximately 1% of those from LBL [23]. A comparison between P1/FSK and P1/Gray reveals the importance (or lack thereof) of spectral radiation properties. And a comparison between P1/FSK and P1/SWG reveals the extent to which the simplified model proposed in [9] is satisfactory for the application of interest. In [9], it was shown that the level of local and global reabsorption predicted by P1/SWG was within approximately 10% of that from PMC/LBL or P1/FSK for a heavy-duty diesel engine, at a small fraction of the computational cost of the latter two models.

## 4 Results

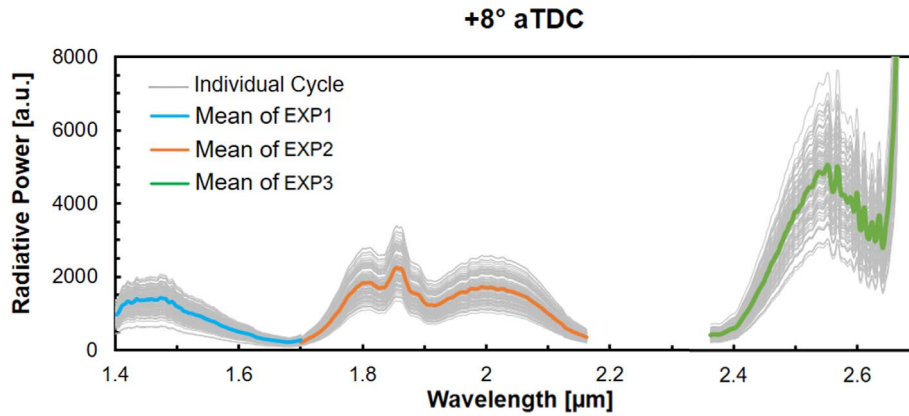
### 4.1 Experimental results

Figure 3 illustrates the 100-cycle phase-average of crank-angle-resolved development of spectral emission reaching the experimental apparatus, hereafter “net radiation”. The net radiation presented contains radiation of H<sub>2</sub>O and CO<sub>2</sub>. The crank-angle-based development of emission from

1.4 to 2.16  $\mu\text{m}$  is composed from two separate experiments, EXP1 and EXP2 (see Tab. 1).

Figure 3 provides an example of the three-dimensional dataset produced by the experimental technique with the engine operating at 1300 rev/min. The vertical axis of these measurements does not have an absolute unit, but rather is a relative measurement with arbitrary units (a.u.). The resulting data is represented as net radiation,  $I_{CA,\lambda}$ , measured every 2.0 CAD between  $-150$  and  $180^\circ$  aTDC for 100 continuous cycles and at wavelengths between 1.4 and 2.16  $\mu\text{m}$ . This data can be examined in different two-dimensional subsets or “slices.” A subset at a constant crank angle gives the radiative power spectrum at the crank angle,  $I_{CA,\lambda}|_{CA=c}$ . A subset at a constant wavelength gives the time-dependent radiative power at that wavelength,  $I_{CA,\lambda}|_{\lambda=c}$ . These relative measurements describe the radiative power throughout the cycle, where zero spectral power represents moments with no measured net radiation.

Figure 4 shows the net radiative spectrum of the 100 individual cycles and the mean of the three experiments described in Table 1 at  $+8^\circ$  aTDC, the crank angle with peak cycle to cycle radiative variation. The spectral variance is substantial; the highest and lowest individual cycles can vary by a factor of four. Individual cycles with above-average radiative power correspond to cycles with faster burn and higher peak pressures. Figure 4 also indicates that the magnitude of radiative variation depends on spectral features, suggesting that the thermodynamic properties might be accessible through the comparison of relative



**Fig. 4.** Average and individual cycle radiative spectrum measured at +8 °aTDC. Radiative variance of spectral features can be seen across the wavelength axis.

radiative spectra. This observation is explored further in what follows.

The average emission across all wavelengths,  $\bar{I}_{CA} = \int \bar{I}_{CA,\lambda} d\lambda$ , was calculated and normalized by the peak value of the ensemble average so it would have a maximum value of 1. The mean net radiation curve and the net radiation curves of the 100 individual cycles of the EXP3 measurements are presented in the top plot of Figure 5. The standard deviation of the EXP3 emission was calculated at all different crank angles to demonstrate when emission varied most. This standard deviation is presented in the bottom plot of Figure 5, and shows peak cycle-to-cycle radiative variation occurred at +8 °aTDC. Mass fraction burn ( $MFB_x$ ) values are combustion landmarks that denote the crank angles where  $x\%$  of the fuel mass had been consumed by the flame. The average  $MFB_{10}$ ,  $MFB_{50}$ , and  $MFB_{90}$  values derived from in-cylinder pressure measurements are shown in Figure 5. Figure 5 shows a relationship between  $MFB_{90}$  and the location of peak radiative. Comparison of the  $MFB_{90}$  value and the location of peak radiative power for the 100 measured cycles yielded a linear correlation of  $R = 0.84$ . Additionally, earlier peak radiative power indicates higher peak radiative power as seen in Figure 5. Therefore, since  $MFB_{90}$  is correlated to peak pressure this implies that higher peak-pressure cycles will have higher net radiation due to increased temperatures in the gas.

While the pressure and radiative power are well correlated, the Cycle-to-Cycle Variation (CCV) of these two metrics is quite different. The Coefficient of Variation (CoV) of peak in-cylinder pressure for EXP3 is 0.066; the CoV of radiative power at the location of peak pressure for EXP3 is 0.105. The CoV at the peak standard deviation of radiative power location for EXP3 is 0.201; similarly, EXP1 and EXP2 have CoVs of 0.197 and 0.218, respectively, at this location. These values show that net radiation varies significantly from cycle to cycle as seen in Figure 4. The standard deviation of spectral emission varies with crank angle, with a peak near  $MFB_{50}$ , as shown on the bottom plot of Figure 5. Significant variation in net radiation occurs during the flame-growth period of the cycle. This

variation could result from the peak temperatures, which are reached during the flame-development period, drastically increasing the radiative power due to its dependence on the *fourth power* of the temperature.

The heat-flux measurements provide information about the timescale of heat flux within a fired cycle. The connection to net radiation is illustrated in Figure 6, which shows the average heat-flux over 100 measured cycles. This plot shows that, while the peak radiative power occurs close to peak heat flux, the radiative heat flux due to the flame reaches the wall before convective heat flux. This result confirms the expectation that radiative heat flux reaches the boundaries of the cylinder faster than convective heat transfer due to the flame. There is a low correlation between the peak heat-flux and peak spectral emission measurements. However, the comparison of these measurements is impacted by the sampling location. Given that the heat-flux measurements happen 35.5 mm away from the optical-measurement axis, as seen in Figure 2, the probe is slower to respond to convective heat flux due to the time needed for the flame to reach the probe.

The right plot of Figure 6 shows the 100-cycle ensemble-averaged Apparent Heat Release Rate (AHRR) for EXP3. The AHRR values were calculated from the in-cylinder pressure measurements. Peak AHRR occurs at +8.5 °aTDC which is near the location of peak radiative variance seen in the bottom plot of Figure 5. The AHRR begins to decrease at the inflection point of the net radiative curve demonstrating a relationship between the AHRR and the measured radiative rate. The growth of AHRR and net radiative power agree qualitatively.

## 4.2 Simulation results

Figure 7 shows the computed pressure traces for each of the 19 LES cycles, the 19-cycle ensemble average cycle, and the measured ensemble average cycle for EXP2. As shown in [21], the computed and measured mean burn rates are in reasonably good agreement, while the LES gives somewhat higher cycle-to-cycle variations compared to the experiment. The pressure traces of the ensemble-averaged cycles

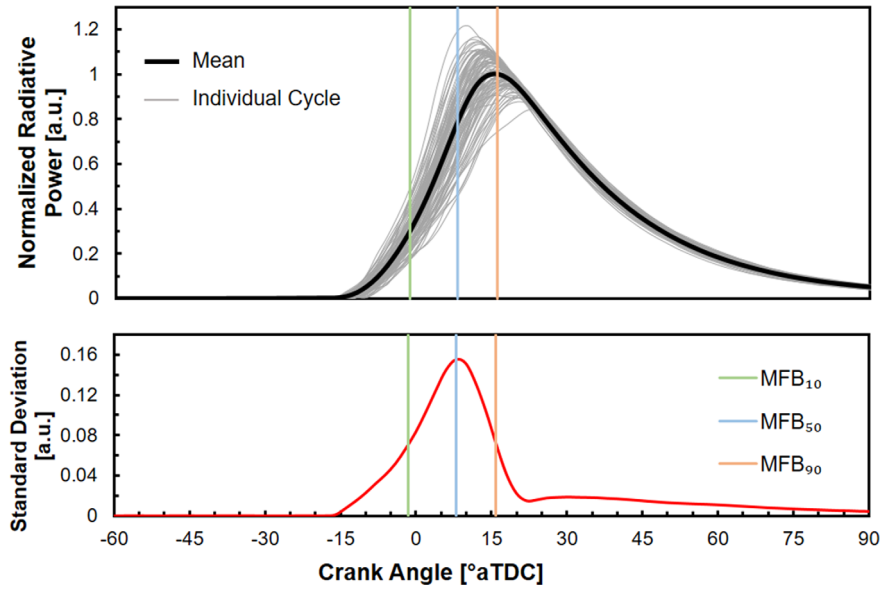


Fig. 5. Top: average and individual cycle net radiative emission against crank angle for EXP3. Bottom: standard deviation of spectral emission against crank angle for radiation from EXP3. 100-cycle average MFB values show flame development.

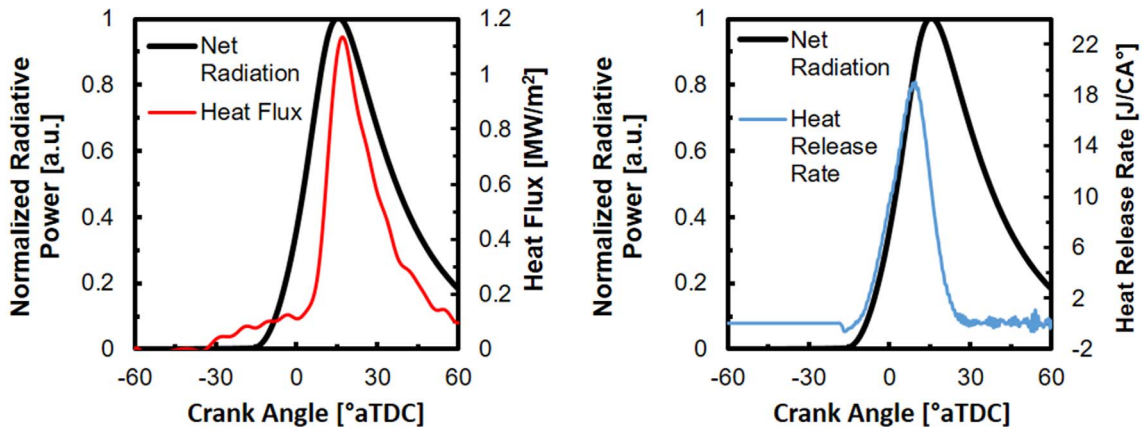


Fig. 6. Heat flux (left plot), heat release rate (right plot), and spectral power measurements throughout an average cycle of EXP3.

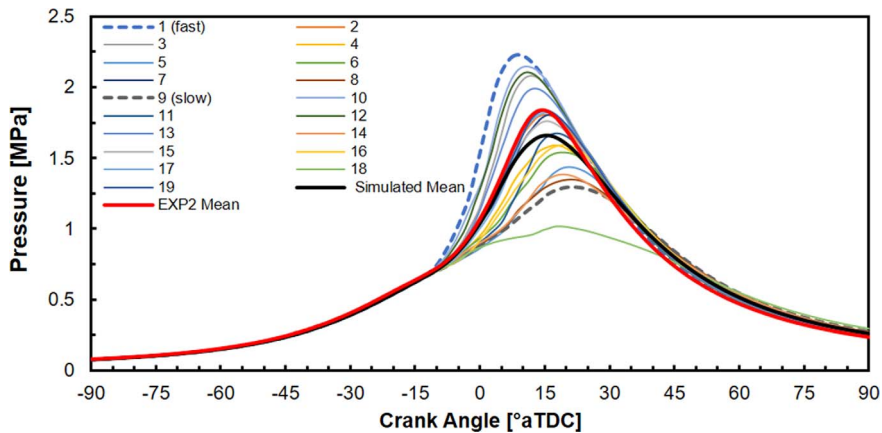
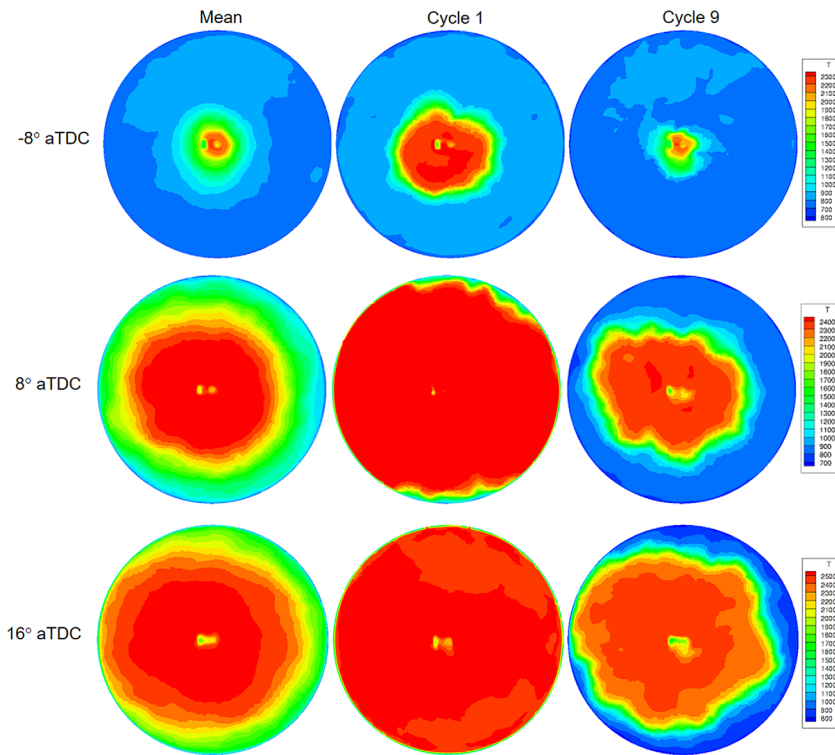


Fig. 7. Computed individual-cycle and mean-cycle in-cylinder pressure traces.



**Fig. 8.** Snapshots of computed temperature fields on a cutting plane normal to the cylinder axis midway between piston and head, at three instants in time: top row at  $-8^\circ$  aTDC; middle row at  $+8^\circ$  aTDC; bottom row at  $+16^\circ$  aTDC. At each instant, three temperature fields are shown: the 19-cycle ensemble-averaged mean (left-hand column), a fast cycle (Cycle 1, middle column), and a slow cycle (Cycle 9, right-hand column).

are added for reference, and show that the mean measured peak in-cylinder pressure is higher than the mean simulated cycle by around 120 kPa. In the subsequent analysis, Cycle 1 is taken as a representative fast cycle and Cycle 9 is taken as a representative slow cycle.

The focus here is on results at three instants in time:  $-8$ ,  $+8$ , and  $+16^\circ$  aTDC. The first corresponds to an early instant in the combustion process, the second to an instant that is close to the peak in the experimentally measured cycle-to-cycle variations in radiative power (Fig. 5), and the third to an instant that is close to the peak in the experimentally measured radiative power (Figs. 5 and 6). Figure 8 provides a visual impression of the location of the flame at each of these three instants, and of the degree of cycle-to-cycle variations in combustion at each instant.

Because of the nonlinear dependence of radiative emission and reabsorption on temperature and composition, the level of spatial resolution in a simulation can affect the computed levels of emission and reabsorption. The influence of mesh resolution on computed total in-cylinder radiative emission and reabsorption is shown in Figure 9 for the P1/FSK model at  $+8^\circ$  aTDC. Results are qualitatively similar at  $-8^\circ$  aTDC and at  $+16^\circ$  aTDC. The fractional changes in the computed total in-cylinder radiative emission and reabsorption are plotted for each cycle, for the 0.5 mm mesh *versus* the 1.0 mm mesh, and for the 1.0 mm mesh *versus* the 2.0 mm mesh. It can be seen that the computed reabsorption is more sensitive to mesh

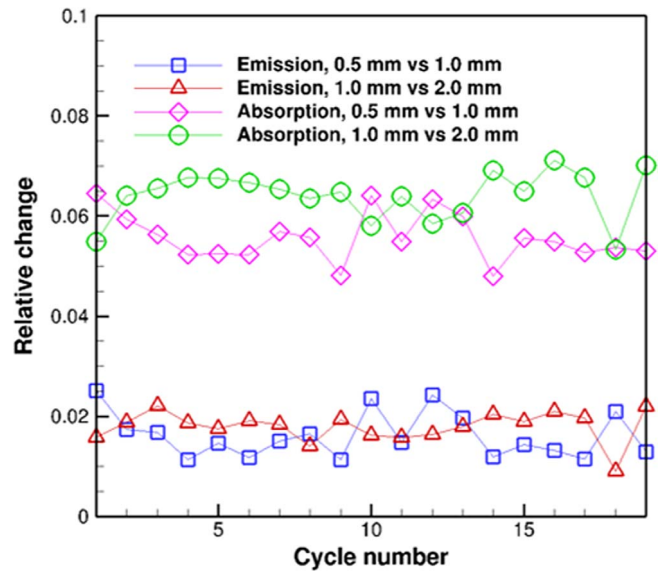


**Fig. 9.** Relative changes in computed total in-cylinder radiative emission and radiative reabsorption (P1/FSK model at  $+8^\circ$  aTDC) using different mesh resolutions, for each cycle.

resolution compared to the computed emission. Also, for most cycles, the differences between the 0.5 mm mesh and the 1.0 mm mesh are smaller than the differences between

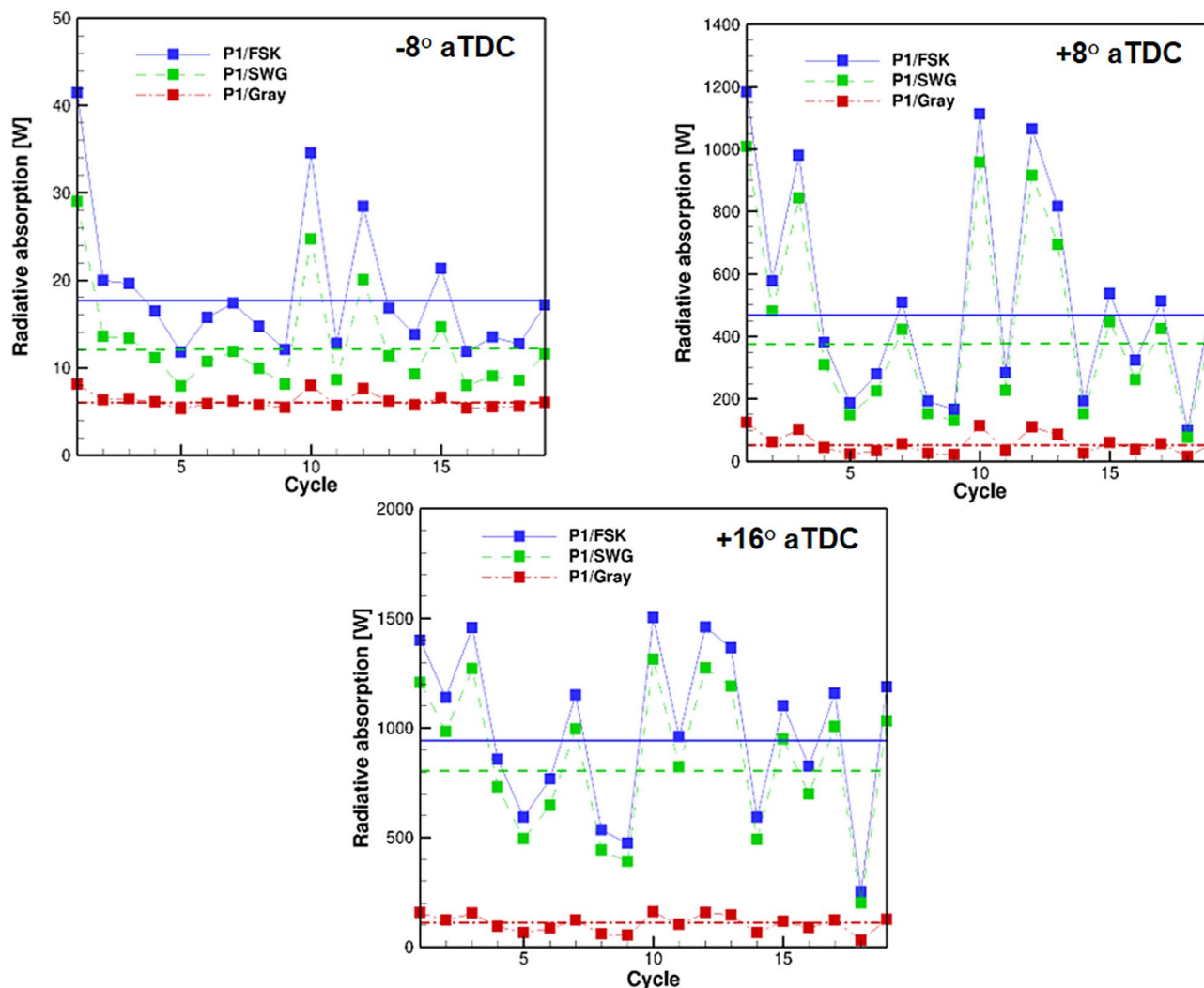


**Fig. 10.** Computed total in-cylinder radiative reabsorption using a 0.5 mm mesh for three radiation models, for each cycle, and at three instants in time. The horizontal lines correspond to radiation calculations based on the ensemble-averaged mean pressure, temperature, and radiatively participating species fields.

the 1.0 mm mesh and the 2.0 mm mesh; this suggests that the results are converging, but finer meshes have not been explored in the present study. As discussed earlier, these are results for approximately uniform meshes, onto which the results from the actual nonuniform LES mesh have been interpolated. The average in-cylinder LES cell size is approximately 0.5 mm, but it is finer in the vicinity of walls and the spark plug. These results suggest that the influences of fluctuations at scales smaller than 0.5 mm (Turbulence-Radiation Interactions [TRI]) on computed radiative reabsorption are greater than the influences on computed radiative emission, but that both are small: less than ~6% for reabsorption, and less than ~2% for emission. All subsequent simulation results are shown for a mesh resolution of 0.5 mm, with the exception of IR spectra, which are computed using the 1.0 mm meshes. Figure 9 also shows that there are large cycle-to-cycle variations, which are explored further in what follows.

The influence of the radiation model is explored in Figure 10. As noted earlier, radiative emission is the same for all models. Also, total P1/FSK reabsorption is within 5% of PMC/LBL reabsorption in all cases; PMC/LBL results are not shown, for clarity. Several observations can be made. First, a gray spectral model underestimates reabsorption by as much as a factor of ~10; consideration of spectral radiative properties is essential. Second, the performance of P1/SWG is not as good here, compared to what was reported in [9], although the P1/SWG reabsorption levels are closer to those from P1/FSK at the later instants in time. This is presumably because in [9], the simplified radiation model was calibrated for heavy-duty-diesel-engine conditions, where pressures are much higher compared to those encountered in this part-load spark-ignition engine. It is anticipated that the parameters in the P1/SWG model (band widths and weights) could be adjusted to give better results in both spark-ignition and diesel engines,

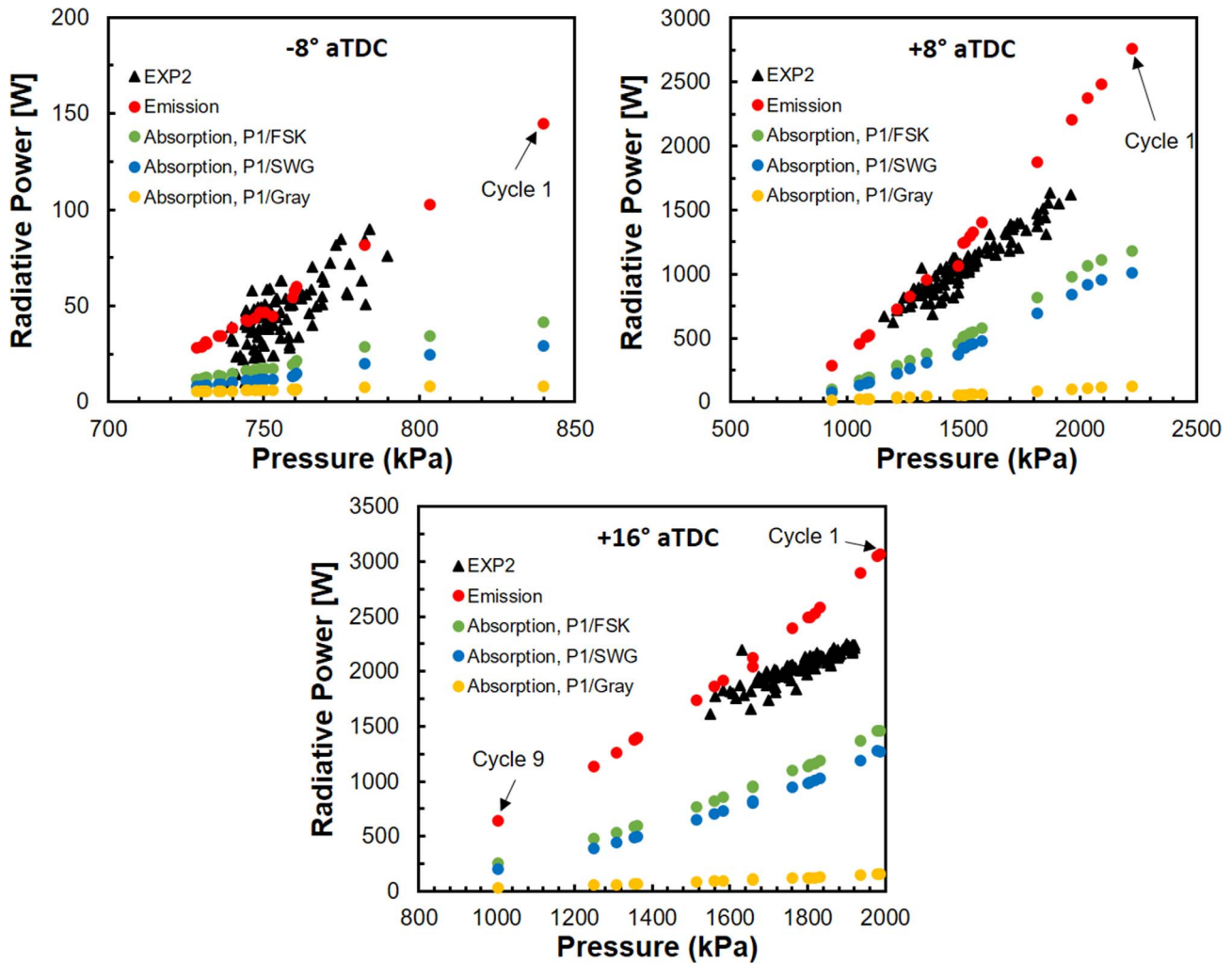


**Fig. 11.** Computed instantaneous total in-cylinder radiative emission and radiative reabsorption *versus* instantaneous in-cylinder pressure using a 0.5 mm mesh for three radiation models, for each individual cycle and the mean cycle, and at three instants in time. Normalized EXP2 measurements of net radiation *versus* instantaneous in-cylinder pressure for all individual cycles.

but that is beyond the scope of the present study. And third, the high degree of cycle-to-cycle variations is again evident.

A close-to-linear correlation is found between the instantaneous computed in-cylinder pressure and the computed total radiative emission and total radiative reabsorption (Fig. 11). The same linear relationship exists for the measured in-cylinder pressure and the measured mean net radiation in the measured cycles. The figure further reinforces the under-prediction of reabsorption by the gray spectral model, and the improved performance of the P1/SWG model with increasing pressure.

Figure 11 also shows that as much as 50% of the radiative energy that is emitted is reabsorbed before reaching a wall. The fraction of emitted radiation that is reabsorbed before reaching a wall ranges from ~30% at -8° aTDC to ~50% at +16° aTDC. In general, the fraction that is reabsorbed increases with increasing concentrations of H<sub>2</sub>O and CO<sub>2</sub>. This implies that radiation acts to

redistribute energy within the combustion chamber, in addition to contributing to heat losses. The fraction of radiative energy that is reabsorbed is much lower here than in the heavy-duty diesel engine considered in [23], though. That is primarily a consequence of the lower in-cylinder pressures here. There is also radiation from soot particles in a diesel engine, but for the conditions considered in [23], molecular gas radiation dominated. Measurements from the mean emission from 1.7 to 2.16 μm region (EXP2) at the three chosen instants were added to the plot. These measurements were scaled so that the mean simulated and measured radiative power were equal. The range of pressures in measurements and simulations pressures is clearly different. Therefore, given linear relationship between the pressure and radiative power, the range of spectral powers seen experimentally is smaller than in simulations. The ranges of radiative power have an influence on the forthcoming comparison between the radiative spectra.

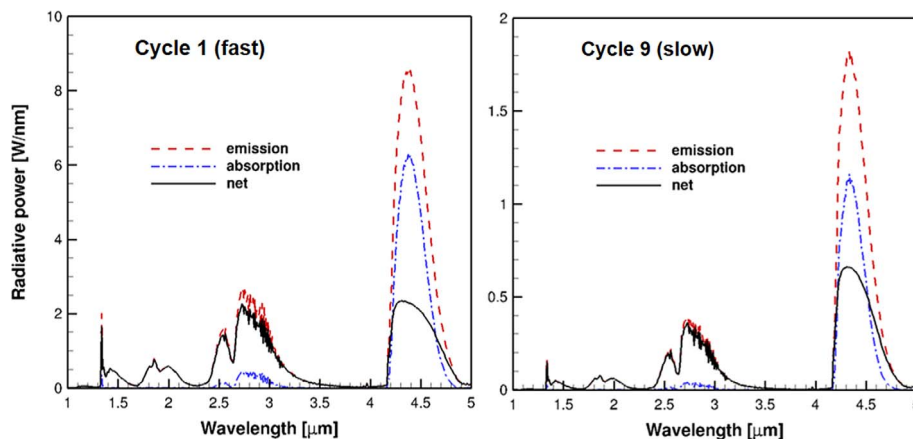


**Fig. 12.** Computed IR spectral radiative intensities from PMC/LBL on the 1 mm mesh at +8 °aTDC for a fast cycle (Cycle 1) and a slow cycle (Cycle 9).

Computed IR spectral intensities of in-cylinder radiation from PMC/LBL for wavelengths between 1 and 5  $\mu\text{m}$  are shown in Figure 12, for a fast cycle (Cycle 1) and for a slow cycle (Cycle 9) at +8 °aTDC. This covers the wavelengths that are relevant for radiative heat transfer under the current in-cylinder conditions. Three spectra are shown for each cycle: the spectrum of the radiation that is emitted, the spectrum of the radiation that is reabsorbed, and the spectrum of the radiation that reaches the walls (labeled “net”). Here the wall is treated as cold and black.  $\text{CO}_2$  has a prominent band centered at approximately 4.4  $\mu\text{m}$  seen in Figure 12. The 4.4  $\mu\text{m}$  band is inaccessible experimentally as the fused-silica liner absorbs the majority of the radiation as shown in Figure 1. The “net” spectrum is the most appropriate to compare with the experimentally measured spectra.

Two observations can be made from Figure 12. First, the reabsorption is strongest in the 4.4  $\mu\text{m}$  band and in the  $\text{H}_2\text{O}/\text{CO}_2$  overlap band at approximately 2.7  $\mu\text{m}$ ; this observation was used to develop the simplified model proposed in [9]. Second, the relative heights of the net spectral peaks are different for the two cycles shown. For example, the ratio of the peak height of the 4.4  $\mu\text{m}$  band to that of the 2.7  $\mu\text{m}$  band is larger for Cycle 9 than for Cycle 1, because of the relatively higher fraction of reabsorption in the 4.4  $\mu\text{m}$  band for Cycle 1 compared to Cycle 9. This is an important observation, as it suggests that one might eventually use the relative heights of the peaks of key spectral bands to back out information on in-cylinder temperature and or composition (equivalence ratio). In the present experiments, the 4.4  $\mu\text{m}$  band is not accessible. For that reason, in Figure 13, we zoom in on the features that are accessible experimentally. There the vertical axis has been scaled to the height of the peak at approximately 2.7  $\mu\text{m}$ . It can be seen that the ratio of the height of the peak at approximately 2.7  $\mu\text{m}$  to that at approximately 1.9  $\mu\text{m}$  is smaller for Cycle 1 than for Cycle 9. This suggests that, even with the limited spectral range that is accessible in the experiments, it might be possible to use the relative height of different spectral peaks to deduce information about the in-cylinder thermochemical environment.

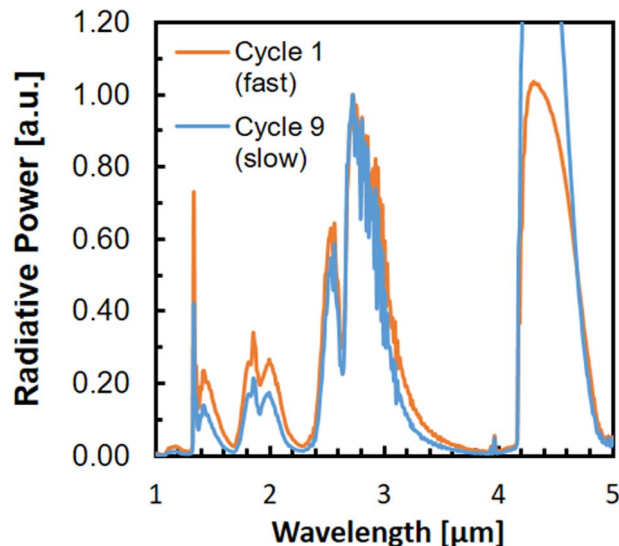


**Fig. 13.** Computed normalized net IR spectral radiative intensities from PMC/LBL on the 1 mm mesh at +8 °aTDC for a fast cycle (Cycle 1) and a slow cycle (Cycle 9). The vertical axis is scaled by the height of the peak at approximately 2.7  $\mu\text{m}$ .

### 4.3 Comparisons between experiments and simulations

Figure 14 shows the comparison of the radiative spectra of the experiments and simulations at  $-8$ ,  $+8$ , and  $+16$  °aTDC. The average simulated net radiation from the simulations is derived from the mean of the 19 simulated cycles; the fast and slow cycle spectra are shown for reference. The measurement data presented is the 100-cycle average from the respective experiments. The simulated spectra are expressed in watts/nm, and the experimental spectra are scaled so that the measured arbitrary units correspond with the simulated units (scaled such that 1 a.u. = 1 watt/nm). All experimental spectra are scaled by the peak value of the simulated spectrum at 1.85  $\mu\text{m}$  at 16 °aTDC, the crank-angle where the peak net radiation occurs. This scaling explains why the spectra at +16 °aTDC

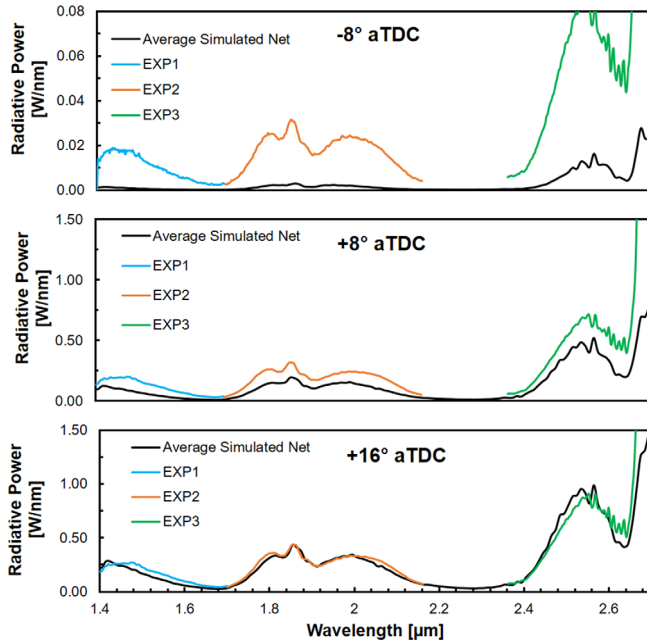


**Fig. 14.** Comparison of measured and simulated IR spectrum from 1.4 to 2.7  $\mu\text{m}$  at  $-8$ ,  $+8$ ,  $+16$   $^\circ\text{aTDC}$ . All measured spectra are normalized by radiative power at 1.85  $\mu\text{m}$  at  $+16$   $^\circ\text{aTDC}$ .

agree well; however, the simulated spectra at  $-8$  and at  $+8$   $^\circ\text{aTDC}$  are under-predicted with this normalization.

The normalization used in Figure 14 shows the crank-angle development of net radiation does not agree between simulations and experiments. The difference between the simulated and experimental probe volumes plays an important role in this discrepancy. The experimental setup captures spectra from a static volume surrounding the flame kernel region. The simulated spectra are the results of volume-averaged integral of flame radiation reaching the wall of engine cylinder. The volume captured in the experiments will tend to bias early flame measurements, and the current scaling shows the early measurements vastly over predict the early simulated spectrum. However, while the time-dependent radiative power magnitudes do not agree well there is strong agreement in the relative radiative spectra.

The agreement of the relative spectral features demonstrates that the PMC/LBL method accurately captures the spectral radiation in the presented wavelength range. In the  $+16$   $^\circ\text{aTDC}$  spectra, there is close agreement between the three major spectral features. Additionally, when the  $-8$  and at  $+8$   $^\circ\text{aTDC}$  are scaled similarly to the simulated spectra at their respective crank angle the same agreement exists. The disparity between the simulated and measured spectra above 2.5  $\mu\text{m}$  is due to the transmission of the fused-silica liner, seen in Figure 5, which amplifies noise and signal due to division by small numbers during correction. For this reason, the measurements above 2.7  $\mu\text{m}$  are omitted. The spectral agreement, along with the previously observed changes of relative spectral features, allows further comparison between the experiments and simulations.

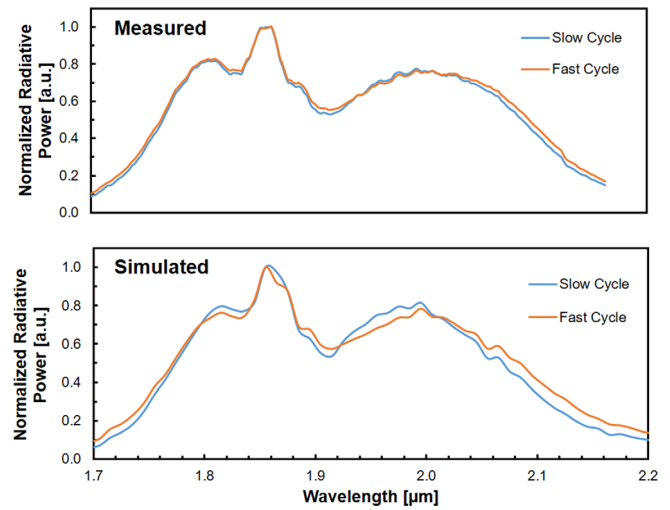


**Fig. 15.** Comparison of fast and slow cycles that are simulated and measured for net radiation from 1.7 to 2.2  $\mu\text{m}$  at 8  $^\circ\text{aTDC}$ . Spectra are normalized at 1.85  $\mu\text{m}$  to illustrate relative spectral differences.

Figure 15 further examines the relative heights of spectral features for slow and fast cycles (high and low peak pressure cycles). The two representative simulated cycles described in the previous section were used, and the measured fast and slow cycles are described in Table 1. EXP2 was chosen because it has radiation features due to  $\text{H}_2\text{O}$  and  $\text{CO}_2$  and has several peaks whose relative features can be compared. To emphasize the change in spectral shape the location of peak radiative variance,  $+8$   $^\circ\text{aTDC}$ , was chosen. These spectra are normalized by the peak radiative power seen around 1.85  $\mu\text{m}$ . There are visible changes in the overall shape of the spectra for fast and slow cycles. Both the measured and simulated fast cycle spectra have larger wings compared to their respective slow cycle. It is important to note that the difference in pressures of the experimental and simulated cycles is quite large. Simulated Cycles 1 and 9 have a 1171 kPa difference of peak in-cylinder pressure; the chosen fast and slow measured cycles have a 673 kPa difference of peak in-cylinder pressure. This difference explains why the measured radiative features demonstrate lesser spectral changes. However, the overall trends in changing spectral features are consistent. This consistency confirms measured spectral sensitivity to the thermo-chemical properties and shows that the simulated spectra are accurately capturing the experimentally observed trends.

## 5 Conclusion

The role and magnitude of radiative heat transfer was investigated for homogeneous stoichiometric propane-fueled operation of the TCC-III engine using Large-Eddy Simulations with various add-on radiation models and high frame rate infrared emissions measurements. Molecular radiation can account for  $\sim 10\%$  of the engine heat loss and could have

a noticeable impact on the local conditions within the combustion chamber. Through this study, it became clear that molecular radiation exhibits significant CCV following the underlying combustion event. Initial steps were taken to validate PMC/LBL simulations of molecular radiation in SI engines with experimental spectra. Spectral features are correctly predicted by the simulations – noting significant restrictions in the experiments for some spectral regions due to strong absorption of the infrared emissions by the quartz cylinder wall of the engine.

Experimental results are scaled to simulated intensities at one crank angle and wavelength position to allow changes with wavelength and crank angle to be easily seen. The temporal evolution differs substantially between simulations and experiments. The net radiation appears under-predicted and this disagreement is likely caused by several sources within the experiments and the simulations. The measured radiative power at  $-8^\circ$  aTDC is low and therefore is subject to higher noise within the experimental apparatus. The net radiation is measured from an imaging volume with a focal point near the spark plug therefore the early flame development is well captured. In contrast the simulations calculate the net radiation as an integral of radiation over the entire cylinder volume and thus at early times have large low-radiation volume portions included while the measurement volume largely contains hot combustion gases. Finally, the mean peak pressure from the simulations was around 6% lower than that of the measurements, implying that the mean measured radiative power would be higher than the simulated mean.

Radiative variance is an important factor in the study of radiative heat transfer in engines. The presented simulations demonstrate that the radiative heat exiting the engine during the flame growth period can vary by a factor of three from cycle-to-cycle and this variance could have noticeable impacts on the local thermal conditions of the in-cylinder gases. The trends of significant radiative variance from cycle-to-cycle and throughout the cycle are consistent between measurements and simulations. Radiative variance primarily occurs during the flame growth period due to the flame development; fast burning cycles reach higher pressures and temperatures resulting in higher net radiation. The peak radiative variance occurs near MFB<sub>50</sub> where the flame has burned half the fuel within the chamber but on average has not reached the boundary of the cylinder. At MFB<sub>50</sub> the net radiation is influenced most strongly by the flame development, and the location where peak AHRR occurs. The flame burnout period, after MFB<sub>90</sub>, has lower radiative variance since temperature differences will be smaller from cycle-to-cycle.

Correlation between relative heights of spectral bands across large wavelength ranges contains information about the temperature and chemical composition of the gas mixture. Temperatures, pressure, and chemical composition influence the spectral lineshape through broadening mechanisms, and the temperature of the gas mixture influences the spectral intensity. Therefore, the thermo-chemical properties of a gas mixture will result in a unique radiative spectrum as observed for fast and slow-burning cycles, implying the conditions are different. The trends seen of the relative

heights of a single vibrational feature between the measurements and the simulation are consistent. This suggests that this measurement technique, which measures in arbitrary units, can be used as a diagnostic of absolute quantities.

*Acknowledgments.* The information, data, or work presented herein was funded in part by the Department of Defense, Tank and Automotive Research, Development and Engineering Center (TARDEC) and the Office of Energy Efficiency and Renewable Energy, U.S. Department of Energy, under Award Number DE-EE0007307. The University of Michigan's Rackham Graduate School provided Mr. Henrion with partial tuition and stipend support *via* the Rackham Merit Fellowship.

## References

- 1 Reitz R.D. (2013) Directions in internal combustion engine research, *Combust. Flame* **160**, 1, 1–8.
- 2 Heywood J.B. (1988) *Internal combustion engine fundamentals*, McGraw-Hill, New York.
- 3 Wiedenhoefer J.F., Reitz R.D. (2003) Multidimensional modeling of the effects of radiation and soot deposition in heavy-duty diesel engines, *SAE Trans.* **112**, 3, 784–804.
- 4 Yoshikawa T., Reitz R.D. (2009) Effect of radiation on diesel engine combustion and heat transfer, *J. Therm. Sci. Technol.* **4**, 1, 86–97.
- 5 Borman G., Nishiwaki K. (1987) Internal-combustion engine heat transfer, *Prog. Energy Combust. Sci.* **13**, 1, 1–46.
- 6 Torregrosa J., Olmeda P.C., Romero C.A., Térmicos M., Valencia U.P.D.E., De Vera C. (2008) Revising engine heat transfer 1, *Ann. Fac. Eng. Hunedoara* **6**, 3, 245–265.
- 7 Fernandez S.F., Paul C., Sircar A., Imren A., Haworth D.C., Roy S., Modest M.F. (2018) Soot and spectral radiation modeling for high-pressure turbulent spray flames, *Combust. Flame* **190**, 402–415.
- 8 Paul C., Sircar A., Fernandez S.F., Imren A., Haworth D.C., Roy S.P., Ge W., Modest M.F. (2017) “Modeling radiative heat transfer and turbulence-radiation interactions in engines”, in U.S., *Nat. Combust. Meet.* **10**, 1–6.
- 9 Paul C., Haworth D.C., Modest M.F. (2019) A simplified CFD model for spectral radiative heat transfer in high-pressure hydrocarbon-air combustion systems, *Proc. Combust. Inst.* **37**, 4617–4624.
- 10 Modest M.F., Haworth D.C. (2016) *Radiative heat transfer in turbulent combustion systems: Theory and applications*, Springer, Berlin, Germany.
- 11 Goldenstein C.S., Spearrin R.M., Jeffries J.B., Hanson R.K. (2017) Infrared laser-absorption sensing for combustion gases, *Prog. Energy Combust. Sci.* **60**, 132–176.
- 12 Rein K.D., Sanders S.T., Lowry S.R., Jiang E.Y., Workman J.J. (2008) In-cylinder Fourier-transform infrared spectroscopy, *Meas. Sci. Technol.* **19**, 4, 1–5.
- 13 Rein K., Sanders S., Bartula R. (2009) Interferometric techniques for crank-angle resolved measurements of gas spectra in engines, *SAE Technical Paper* (No. 2009-01-0863), 1–7.
- 14 Rein K.D., Sanders S.T. (2010) Fourier-transform absorption spectroscopy in reciprocating engines, *Appl. Opt.* **49**, 25, 4728–34.
- 15 Sick V., Henrion L., Mazacioglu A., Gross M.C. (2018) Time-resolved infrared imaging and spectroscopy for engine diagnostics, in: *13th AVL Intl. Symp. on Propulsion Diagnostics Proceedings*, AVL GmbH, Austria.

- 16 Schiffmann P., Reuss D.L., Sick V. (2018) Empirical investigation of spark-ignited flame-initiation cycle-to-cycle variability in a homogeneous charge reciprocating engine, *Int. J. Engine Res.* **19**, 5, 491–508.
- 17 Humphreys C.J., Paul E. (1970) Interferometric Wavelength Determinations in the First Spectrum of  $^{136}\text{Xe}$ , *J. Opt. Soc. Am.* **60**, 10, 1302–1310.
- 18 Ma P.C., Greene M., Sick V., Ihme M. (2017) Non-equilibrium wall-modeling for internal combustion engine simulations with wall heat transfer, *Int. J. Engine Res.* **18**, 15–25.
- 19 Oude Nijeweme D.J., Kok J.B.W., Stone C.R., Wyszynski L. (2001) Unsteady in-cylinder heat transfer in a spark ignition engine: Experiments and modelling, *Proc. Inst. Mech. Eng. Part D J. Automob. Eng.* **215**, 6, 747–760.
- 20 Herzberg G. (1945) *Infrared and Raman spectra of polyatomic molecules*, D. Van Nostrand Company, New York City.
- 21 Shekhawat Y., Haworth D.C., d'Adamo A., Berni F., Fontanesi S., Schiffmann P., Reuss D.L., Sick V. (2017) An experimental and simulation study of early flame development in a homogeneous-charge spark-ignition engine, *Oil Gas Sci. Technol. - Rev. IFP Energies nouvelles* **72**, 32.
- 22 Weller H., Greenshields C., de Rouvray C., OpenFoam. (2011) *The OpenFOAM Foundation*. [Online]. Available: <https://openfoam.org/>
- 23 Paul C., Ferreyro-Fernandez S., Haworth D.C., Roy S., Modest M.F. (2019) A detailed modeling study of radiative heat transfer in a heavy-duty diesel engine, *Combust. Flame* **200**, 325–341.
- 24 Rothman L.S., Gordon I.E., Barber R.J., Dothe H., Gamache R.R., Goldman A., Perevalov V.I., Tashkun S.A., Tennyson J. (2010) HITEMP, the high-temperature molecular spectroscopic database, *J. Quant. Spectrosc. Radiat. Transf.* **111**, 15, 2139–2150.